THE BALTIC JOURNAL
OF ROAD AND BRIDGE ENGINEERING
2026/21(3)

ISSN 1822-427X/eISSN 1822-4288
2026 Volume 21 Issue 3: 41–76
https://doi.org/10.7250/bjrbe.2026-21.682

SHEAR CAPACITY AND DAMAGE EVOLUTION OF NEW-TO-OLD CONCRETE INTERFACES UNDER TRAFFIC-INDUCED VIBRATION

BAISHUN XU[1], MING MA[2], TIANMENG NI[3], CHUAN XIAO[4,*], MIAO ZHANG[4]

[1] *School of Civil Engineering and Architecture, Suqian University, Suqian, Jiangsu, China*

[2] *CCCC First Highway Consultants Co., Ltd, Xi'an, China*

[3] *Inner Mongolia Communications Design and Research Institute Co., LTD., Hohhot, China*

[4] *Sichuan University of Architectural Technology, Deyang, Sichuan, China*

Received 7 January 2026; accepted 28 August 2026

Abstract. To investigate the effects of traffic-induced vibration on the shear performance and damage evolution of new-to-old concrete interfaces, eight groups of composite specimens with different curing ages were designed and fabricated, and a six-degree-of-freedom shaking table was used to simulate vehicle-induced vibration. Based on test results and acoustic-emission (AE) characteristics, a modified shear-capacity model incorporating vibration effects was established. In addition, the damage evolution of the interface was systematically revealed using an energy-based approach, RA-AF correlation analysis, and fuzzy C-means clustering. The results show that vibration applied during the early setting stage leads to an initial increase and subsequent decrease in interfacial shear capacity. The

* Corresponding author. E-mail: xcaaa6666@sina.com

Baishun XU (ORCID ID 0009-0005-5760-6745)
Ming MA (ORCID ID 0000-0003-0743-3776)
Tianmeng NI (ORCID ID 0009-0003-9594-488X)
Chuan XIAO (ORCID ID 0009-0007-7072-2147)
Miao ZHANG (ORCID ID 0009-0006-5570-5747)

fuzzy C-means clustering. The results show that vibration applied during the early setting stage leads to an initial increase and subsequent decrease in interfacial shear capacity. The proposed modified model agrees well with the experimental measurements. According to the distribution of cumulative AE energy, the damage process can be divided into three stages: an elastic stage, a cracked-working stage, and a failure stage. Damage evolution is dominated by crack initiation and propagation at the interface and within the concrete matrix, which together account for more than 90% of the overall damage. The interfacial damage is primarily tensile in nature, with an event occurrence rate exceeding 75%, and the rise time of failure-related signals mainly falling within 0–200 μs.

Keywords: acoustic emission, interface, new-to-old concrete, shear capacity, traffic-induced vibration.

Introduction

By the end of 2023, a total of 1.08 million highway bridges had been constructed in China (Editorial Department of China Journal of Highway and Transport, 2024). Under the combined long-term influence of mechanical loads and environmental factors, concrete bridges experience marked material degradation, progressively weakening their structural capacity (Ibrahim et al., 2024; Li et al., 2022). With the continuous growth of traffic demand, the widening and reconstruction of existing bridges have become important measures to enhance transportation capacity (Shao et al., 2019; Xu et al., 2021). Bridge widening generally requires the connection of the superstructures of new and existing bridges. For concrete bridges, the shear capacity of the interface between new and old concrete plays a critical role in ensuring the structural integrity and safety of widened bridges (Cattaneo et al., 2021; Maili & Jing, 2018).

Extensive studies have been conducted on the shear performance of new-to-old concrete interfaces (Daneshvar et al., 2022). A variety of test methods were employed, including tensile (Momayez et al., 2005; Zanotti & Randl, 2019), shear (Jang et al., 2017; Santos et al., 2012), tensile-shear (Feng et al., 2020) and compression-shear tests (Liu et al., 2024). Based on a literature survey, Júlio et al. noted that most calculation methods for the bond strength at the new-to-old concrete interface proposed by scholars share a common foundation in the shear friction theory (Júlio et al., 2010). Lin et al. analyzed the applicability of existing shear capacity calculation methods for new-to-old concrete interfaces and proposed a more effective formula based on a spring-friction block model (Lin et al., 2021). Bai et al. investigated the effects of surface treatment methods and roughness on the shear behavior of new-to-old concrete interfaces through direct shear tests and established a shear strength model considering segmented roughness and different surface treatment techniques (Bai et al., 2024). Yan et al. constructed a shear capacity database and trained six machine learning models, demonstrating that machine learning-based predictions significantly outperform traditional empirical formulas (Yan et al., 2025). Huang et al. explored the shear performance of new-to-old concrete interfaces at the nanoscale using molecular dynamics simulations (Huang et al., 2025). These studies have substantially advanced the understanding of interfacial shear behavior in composite concrete structures.

However, bridge widening projects are often carried out under open or intermittently open traffic conditions, during which the newly cast concrete is inevitably subjected to traffic-induced vibration (Zhou et al., 2023). Research on the influence of traffic vibration on the shear capacity of new-to-old concrete interfaces remains limited. Wei et al. investigated the tensile strength of new-to-old concrete interfaces under three different traffic vibration conditions (Wei et al., 2016). Gu et al. studied the effects of traffic-induced vibration on the tensile strength of new-to-old concrete interfaces through vibration tests and theoretical analysis (Gu et al., 2024). In contrast, systematic investigations of the shear behavior of new-to-old concrete interfaces under traffic vibration remain scarce.

Acoustic emission (AE) technology is an important nondestructive technique for damage detection and evaluation in concrete materials (Tsangouri & Aggelis, 2019). Kocáb et al. systematically described the basic principles, characteristic parameters, and damage quantification methods of AE technology for cement-based materials (Kocáb et al., 2019). Li et al. proposed AE-based damage evaluation and precise damage source localization methods for concrete under different stress levels (Li et al., 2025). Nevertheless, the application of AE techniques to the damage analysis of new-to-old concrete interfaces has rarely been reported.

To investigate the effects of traffic-induced vibration disturbance on the load-carrying capacity of new-to-old bridge interfaces, this study takes the new-to-old concrete interface as the research object. Direct shear tests are conducted on post-installed rebar Z-shaped specimens subjected to vibration disturbance at different curing ages. Combined with acoustic emission monitoring, the influence of vibration disturbance on the shear capacity of the interface is revealed; an existing shear capacity formula is modified, and the damage evolution characteristics of the interface are systematically analyzed.

1. Bridge vibration characteristics and determination of test parameters

Bridge widening commonly requires new concrete to be cast while traffic on the existing bridge remains open or is interrupted only intermittently. Dynamic responses generated by vehicles crossing the existing span are transmitted to the new-to-old concrete connection, disturbing the new concrete during its setting and hardening (Zhou et al., 2023). Actual traffic-bridge interaction varies with vehicle type, speed, axle load, pavement roughness, and vehicle distribution, and therefore exhibits pronounced time-dependence and randomness (Gu et al., 2024; Qiao et al., 2025). A single harmonic excitation cannot fully reproduce such responses. Rather than reconstructing the complete response history of a specific vehicle passage, this study extracts representative frequency and displacement scales from typical bridge responses. These scales provide repeatable vibration inputs for the subsequent controlled experiments. Full-bridge finite element models of typical short- and medium-span simply supported prestressed concrete T-girder bridges were established in Midas Civil. Eigenvalue and static vehicle-load analyses were then conducted to obtain the vertical fundamental frequency, maximum static deflection, and maximum dynamic deflection after code-specified dynamic amplification.

1.1. Finite element models of bridge

Simply supported prestressed concrete T-girder bridges with standard spans of 16 m, 20 m, 25 m, 30 m, 35 m, and 40 m were selected. This range covers short- and medium-span bridges commonly encountered in highway widening projects. Table 1 summarizes the standard span (L), effective span (L_0), girder length (l), girder depth (h), and number of diaphragms. To isolate the effect of span length on dynamic characteristics, all models used the same transverse deck arrangement and analysis procedure, with only span-dependent geometric parameters varied.

Table 1. Mixture proportion of concrete

Standard span L, m	Effective span L_0, m	Girder length l, m	Girder depth h, m	Number of diaphragms
16	15.50	15.96	1.30	4
20	19.50	19.96	1.50	5
25	24.28	24.96	1.75	6
30	29.14	29.96	2.00	7
35	34.00	34.96	2.25	8
40	38.86	39.96	2.50	9

Figure 1 shows the general layout and finite element model of the bridges. Each simply supported T-girder bridge had two traffic lanes with a total carriageway width of 7.0 m and 0.5 m wide barriers on both sides. A beam-grillage model of one simply supported span was established in Midas Civil. The main girders and diaphragms were represented by beam elements, while zero-weight beam elements were used as dummy transverse members. The C50 concrete had a standard axial compressive strength of 32.4 MPa and an elastic modulus of 3.45×10^4 MPa. The unit weight of the concrete was 26 kN/m^3. High-strength, low-relaxation prestressing strands with a nominal diameter of 15.2 mm had a standard tensile strength of 1860 MPa and an elastic modulus of 1.95×10^5 MPa. The HRB400 reinforcing steel had a standard tensile strength of 400 MPa and an elastic modulus of 2.0×10^5 MPa. Each girder was supported by one fixed bearing and one movable bearing.

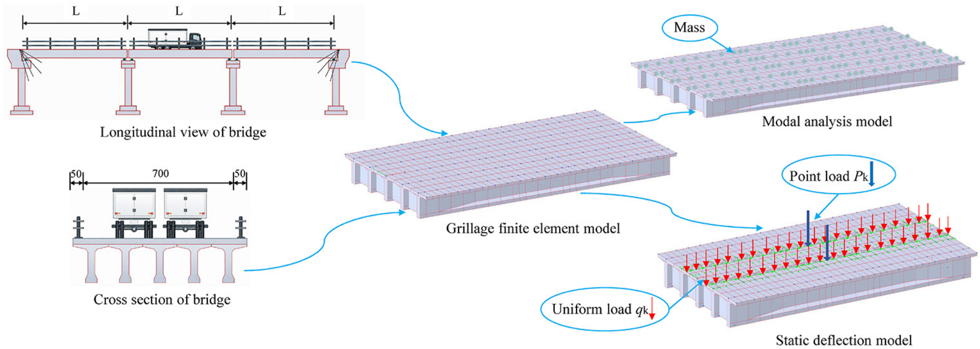

Figure 1. General layout and finite element model of the bridge

1.2. Natural vibration characteristics

The traffic-induced response of a bridge is a non-stationary forced vibration, and its instantaneous dominant frequency is not identical to the natural frequency of the structure. The forced-vibration frequency varies with vehicle operating conditions, and the dynamic response is maximized when the excitation frequency approaches a natural frequency. Accordingly, the fundamental frequency f associated with the first vertical bending mode was used as the principal reference for selecting the laboratory excitation frequency.

For each beam-grillage model, the structural mass was first defined by converting self-weight and external loads into mass, as illustrated by the modal-analysis model in Figure 1. The eigenvalue analysis used the Lanczos method and extracted the first-order mode. The first vertical bending mode and its corresponding frequency were then obtained, and the results are listed in Table 2. As the standard span increased from 16 m to 40 m, the vertical fundamental frequency decreased monotonically from 8.21 Hz to 2.42 Hz. This trend reflects the relationship between the overall vertical stiffness and mass as the span increases.

Table 2. Vibration characteristics of the bridges

Standard span L, m	Fundamental frequency f, Hz	Maximum static deflection y_s, mm	Impact factor μ	Maximum dynamic deflection y_d, mm
16	8.21	0.72	0.356	0.98
20	6.38	1.61	0.312	2.11
25	5.94	3.10	0.299	4.03
30	4.46	5.21	0.248	6.50
35	3.78	7.20	0.219	8.78
40	2.42	8.63	0.140	9.84

1.3. Maximum dynamic deflection under vehicle loading

The dynamic deflection of a bridge can be estimated using the impact-factor method. The ratio of the maximum dynamic deflection to the maximum static deflection at a given location is expressed as

$$1+\mu = y_d / y_s, \tag{1}$$

where y_d is the maximum dynamic deflection, y_s is the corresponding maximum static deflection, and μ is the impact factor. Equation (1) can be rearranged as

$$y_d = (1+\mu)\cdot y_s. \tag{2}$$

The impact factor μ was calculated according to the General Specifications for Design of Highway Bridges and Culverts (JTG D60-2015) (Ministry of Transport of the People's Republic of China, 2015):

$$f < 1.5\ \text{Hz};\quad \mu = 0.05, \tag{3}$$

$$1.5\ \text{Hz} \le f \le 14\ \text{Hz};\ \mu = 0.1767 \ln f - 0.0157, \tag{4}$$

$$f > 14\ \text{Hz};\quad \mu = 0.45. \tag{5}$$

Here, f is the structural fundamental frequency obtained in Section 1.2. The fundamental frequencies of all six bridges lie between 1.5 Hz and 14 Hz; therefore, Equation (4) applies to every model. The resulting impact factors range from 0.140 to 0.356, as listed in Table 2.

The maximum static deflection y_s was obtained from the Midas Civil models shown in Figure 1. Highway Class-I lane loading was applied in accordance with the General Specifications for Design of Highway Bridges and Culverts (JTG D60-2015) (Ministry of Transport of the People's Republic of China, 2015). The lane loading comprised a uniformly distributed load and a concentrated load. The standard uniformly distributed load was $q_k = 10.5$ kN/m. For effective spans L_0 between

5 m and 50 m, the standard concentrated load was $P_{\mathrm{k}} = 2(L_0 + 130)$ kN. Deflection was evaluated using the frequent combination of actions at the serviceability limit state. This procedure followed the Specifications for Design of Highway Reinforced Concrete and Prestressed Concrete Bridges and Culverts (JTG 3362-2018) (Ministry of Transport of the People's Republic of China, 2018):

$$\omega_{\mathrm{fd}} = \sum \omega_{Gik} + \psi_{f1}\omega_{1k} . \tag{6}$$

Here, ω_{fd} is the design deflection under the frequent combination of actions. The term $\sum\omega_{\mathrm{G}ik}$ is the total deflection induced by the characteristic values of all permanent actions, including self-weight and prestressing. The term $\omega_{1\mathrm{k}}$ is the deflection induced by the characteristic vehicle load without the impact effect. The frequent-value factor ψ_{f1} for vehicle loading is specified as 0.7. Moving-load analysis was used to obtain the vertical displacement envelope for each span. The maximum absolute value in the midspan region was taken as y_{s}, as listed in Table 2. The maximum dynamic deflection y_{d} was then calculated using Equation (2) and is also reported in Table 2.

This procedure represents the dynamic amplification of vehicle loading through the code-specified impact factor. Therefore, y_{d} is an equivalent design response rather than an instantaneous displacement obtained from a traffic-bridge interaction time-history analysis.

1.4. Test vibration parameters

As shown in Table 2, the vertical fundamental frequencies of the six bridges range from 2.42 Hz to 8.21 Hz. Their maximum dynamic deflections range from 0.98 mm to 9.84 mm. The 20 m span model has a fundamental frequency of 6.38 Hz, while the 25- and 30-m-span models have maximum dynamic deflections of 4.03 mm and 6.50 mm, respectively. An excitation frequency of 6 Hz and a displacement amplitude of 5 mm therefore fall within the frequency-deflection ranges obtained from the finite element analyses. These values are also close to the fundamental frequency of the 20 m bridge and the representative dynamic deflections of the 25- and 30-m bridges. Moreover, this combination lies within the traffic-vibration ranges of 2-10 Hz and 1-10 mm reported in the literature (Wei et al., 2016). Therefore, the subsequent tests on Z-shaped new-to-old concrete composite specimens used an excitation frequency of 6 Hz and a displacement amplitude of 5 mm. The selected parameters balance engineering representativeness and laboratory repeatability.

2. Materials and experiments

2.1. Materials

The old concrete was designed with strength grade C30, while the new concrete adopted strength grade C40. Ordinary Portland cement (P O 42.5) was used for both concretes. The coarse aggregate consisted of mechanically crushed stone with a particle size ranging from 4.75 mm to 26.5 mm. Medium sand with a particle size of 0.15-4.75 mm was used as the fine aggregate. A polycarboxylate superplasticizer with a water-reducing rate of 30% was incorporated at a dosage of 1% by weight of cement. The material proportions and mix designs of the new and old concretes are summarised in Table 3.

Table 3. Mixture proportion of concrete

Name	Grade	Water-cement ratio	Materials consumption, kg/m^3			
			Cement	Coarse aggregate	Fine aggregate	Water
Old concrete	C30	0.43	460.4	1015.0	676.7	198.0
			1	2.20	1.47	0.43
New concrete	C40	0.40	554.2	965.5	643.3	221.6
			1	1.74	1.16	0.40

2.2. Specimen preparation

According to the relevant provisions for Concrete Mixing on determining concrete setting time using a penetration resistance tester, the relationship between penetration resistance and time was experimentally obtained, as shown in Figure 2. When the penetration resistance was lower than 3.5 MPa, the concrete was considered to be in the initial setting stage, corresponding to a curing time of 0–4.5 h. When the penetration resistance ranged from 3.5 MPa to 28 MPa, the concrete was in the transition stage from initial setting to final setting, corresponding to a curing time of 4.5–7.5 h.

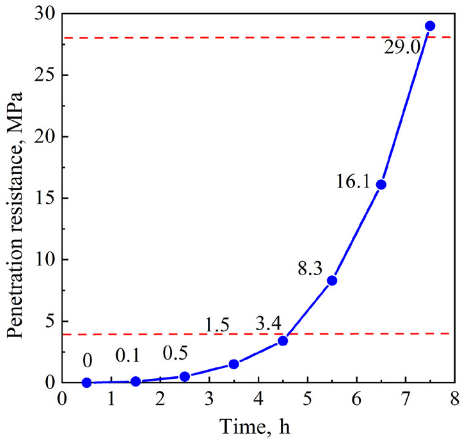

Figure 2. Penetration resistance-time curves

A total of eight groups of specimens were prepared, with three specimens in each group, resulting in 24 concrete cube specimens with dimensions of 150 mm × 150 mm × 150 mm, as well as post-installed rebar new-to-old concrete Z-shaped specimens with dimensions of 100 mm × 300 mm × 400 mm, as shown in Figure 3. The Z-shaped specimens were cast in two stages. First, the old concrete part was poured and cured for 28 days. The surface was then roughened by chiseling, washed with high-pressure water, and air-dried. After the surface was completely dry, the new concrete part was cast.

The specimen group identification is listed in Table 4. The naming convention "D-X" was adopted, where "D" denotes the concrete cube specimens and "X" represents the curing age at which vibration disturbance was applied. For example, "D-0.5" indicates that vibration disturbance was applied to the cube specimens after 0.5 h of curing. Similarly, in the designation "ZJ-X", "ZJ" denotes the post-installed rebar new-to-old concrete specimens, and "X" represents the curing age at which vibration disturbance was applied. For instance, "ZJ-0.5" indicates that vibration disturbance was applied to the post-installed rebar specimens after 0.5 h of curing. Specimens D-0 and ZJ-0, which were not subjected to vibration disturbance, were taken as the reference group.

During the fabrication of the new-to-old concrete specimens, the old concrete (C30) part was first cast and cured for six months. Subsequently, formwork was installed, and the new concrete (C40) part was cast. After vibration disturbance, both types of specimens were cured in molds in a constant-temperature and constant-humidity curing chamber (20 ± 2 °C, RH ≥ 95%) for 28 days. Two

HPB300-grade steel rebars with a diameter of 12 mm were embedded in each specimen, with an embedment depth of 120 mm.

Table 4. Specimen group number

Number	Cube	New-to-old	Curing age, h
1	D-0	ZJ-0	0
2	D-0.5	ZJ-0.5	0.5
3	D-1.5	ZJ-1.5	1.5
4	D-2.5	ZJ-2.5	2.5
5	D-3.5	ZJ-3.5	3.5
6	D-4.5	ZJ-4.5	4.5
7	D-5.5	ZJ-5.5	5.5
8	D-6.5	ZJ-6.5	6.5

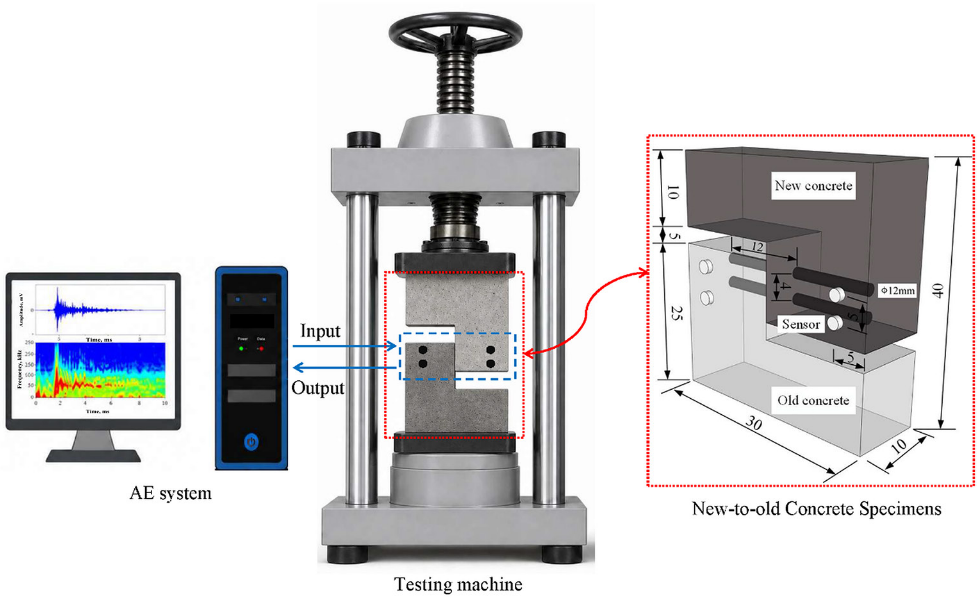

Figure 3. Testing equipment and New-to-old concrete specimens, dimensions in cm

2.3. Experimental programme

Based on the findings in Section 1.4, the vibration parameters adopted in this study were selected as a frequency of 6 Hz, an amplitude of 5 mm, and a vibration duration of 30 min. The excitation system consisted of a Hexapod six-degree-of-freedom shaking table, as shown in Figure 4. The loading system for the mechanical tests was a TYA-2000 closed-loop servo-controlled hydraulic testing machine. The acoustic emission (AE) monitoring system comprised a PAC Micro II Express multichannel digital acquisition system and DT15I-AST broadband sensors. The trigger threshold was set to 35 dB (signal-to-noise ratio ≥ 6 dB), the preamplifier gain was 40 dB with a bandwidth of 100 kHz ~ 2 MHz, and the digital filter was configured in band-pass mode with a frequency range of 100~400 kHz. The layout of the AE sensors is illustrated in Figure 3. The loading rate was controlled at 0.2 mm/min.

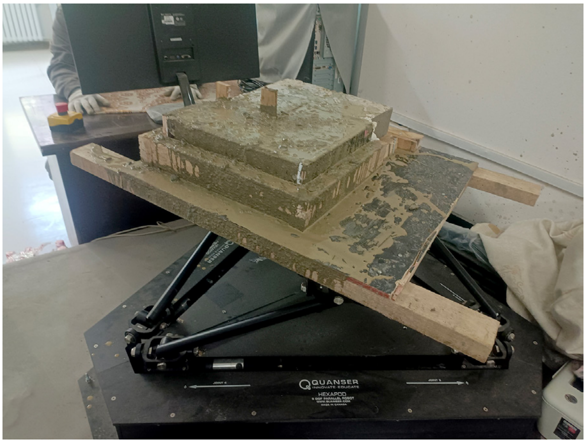

Figure 4. Six-degree-of-freedom shaking table

3. Results and analysis

3.1. Concrete cube specimens

The compressive strengths of concrete cube specimens subjected to vibration at different curing ages are listed in Table 5. For each group, the average compressive strength of three specimens was calculated and plotted as a bar chart, as shown in Figure 5. Comparison of the data in Table 5 and the results in Figure 5 indicates that vibration applied at different curing ages noticeably influences the compressive strength of concrete.

Compared with the reference group D-0, the compressive strength of specimens subjected to vibration before the curing age of 2.5 h (i.e., up to group D-2.5) exhibits an increasing trend, followed by a gradual decrease. A slight increase is observed again for group D-6.5. In other words, vibration applied before a curing age of 2.5 h contributes to an improvement in compressive strength compared with the reference group, with a maximum increase of 12.4%.

This phenomenon can be attributed to the fact that concrete is in a plastic stage at early ages and exhibits pronounced thixotropic behavior. Vibration disturbance during this stage accelerates the rearrangement of the cementitious system, promoting the effective filling of voids between coarse aggregates by the cement paste and fine aggregates. As a result, the interfacial transition zone becomes denser, leading to an enhancement in compressive strength.

When the curing age exceeds 2.5 h, the thixotropic recovery capacity of the cementitious system gradually weakens. Under such conditions, vibration disturbance induces stress concentration at the aggregate-paste interface, which in turn leads to a reduction in compressive strength. Compared with the reference group, the compressive strength of group D-5.5 decreases by up to 13.2%. When the curing age exceeds 6.5 h, the concrete exhibits an improved resistance to disturbance, and the compressive strength shows a partial recovery.

Table 5. Compressive strength of concrete

Number	No.1, MPa	No.2, MPa	No.3, MPa	Average, MPa
D-0	47.6	46.0	48.8	47.5
D-0.5	52.7	49.3	50.3	50.8
D-1.5	51.5	53.0	53.6	52.7
D-2.5	53.2	53.5	53.5	53.4
D-3.5	46.9	49.9	46.1	47.6
D-4.5	45.0	46.0	45.2	45.4
D-5.5	40.0	41.9	41.7	41.2
D-6.5	41.0	42.0	42.6	41.9

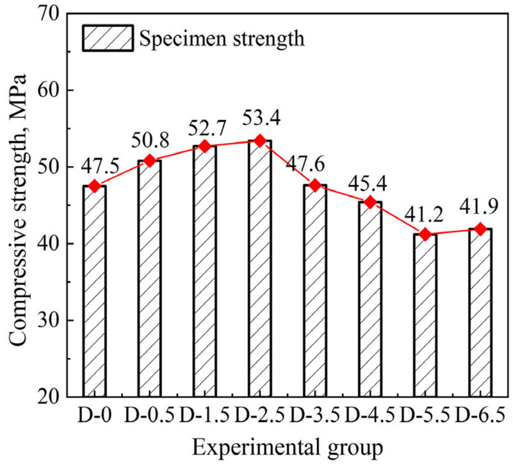

Figure 5. Average compressive strength

3.2. New-to-old concrete specimens

The failure processes of all specimen groups are generally similar. At low load levels, the specimens remain in an elastic working state. When the applied load reaches the cracking load, slight cracking sounds can be heard, and vertical cracks initiate at the interface between the new and old concrete. With further increases in load, the cracks gradually widen and propagate along the entire interface, while the relative displacement between the new and old concrete parts continues to increase.

When the ultimate load is reached, the specimens fail. Owing to the anchoring effect of the post-installed rebars, complete separation between the new and old concrete does not occur. The failure process exhibits clear characteristics of plastic failure. Typical failure patterns of the specimens are shown in Figure 6.

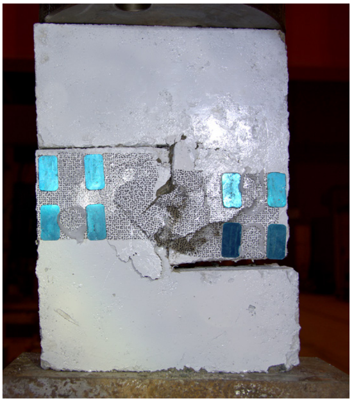

Figure 6. Specimen failure

The shear capacities of the new-to-old concrete specimens subjected to vibration at different curing ages are summarised in Table 6. For each group, the average shear capacity of three specimens was calculated and presented in the form of a bar chart, as shown in Figure 7. Comparing the data in Table 6 with the results in Figure 7 indicates that the trend in shear capacity generally matches that observed for the compressive strength of the concrete cube specimens.

The difference lies in that the influence of vibration disturbance on shear capacity is mainly associated with the setting and hardening process of the new concrete, the formation of the new-to-old concrete interface, and the stirring effect induced by the post-installed rebars on the freshly cast concrete. Among all groups, specimen group ZJ-2.5 exhibits the highest shear capacity, showing an increase of 26.6% compared with the reference group ZJ-0. In contrast, specimen group ZJ-5.5 shows the lowest shear capacity, with a reduction of 12.4% relative to the reference group ZJ-0.

Table 6. Shear capacity

Number	No.1, kN	No.2, kN	No.3, kN	Average, kN	Calculation, kN	*K*, %
ZJ-0	50.8	54.0	55.4	53.4	53.4	0
ZJ-0.5	63.2	60.5	58.4	60.7	61.8	13.7
ZJ-1.5	66.0	67.3	65.6	66.1	68.1	24.1
ZJ-2.5	65.8	68.1	68.9	67.6	69.7	26.6
ZJ-3.5	56.7	57.9	57.6	57.4	57.5	7.5
ZJ-4.5	50.6	52.3	51.3	51.4	50.9	–3.8
ZJ-5.5	49.1	47.0	44.3	46.8	45.3	–12.4
ZJ-6.5	47.2	49.9	45.7	47.6	46.3	–10.8

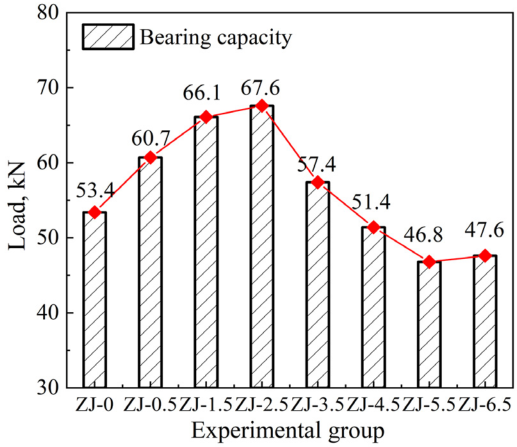

Figure 7. Average shear capacity

3.3. Calculation of shear capacity

According to the latest research results reported by Lin et al. (Lin et al., 2021), the shear capacity of the new-to-old concrete interface, denoted as V_u, can be expressed as

$$V_u = V_{BO,F} + V_{KB,F} + V_{PI,F} + V_{FRI}, \tag{7}$$

where $V_{BO,F}$ is the bonding force; $V_{KB,F}$ is the shear resistance provided by key-slot interlocking; $V_{PI,F}$ represents the dowel action of the post-installed rebars; andV_{FRI} is the frictional resistance. Since no key slots were formed in the specimens used in this study, the term $V_{KB,F}$ is not considered. The remaining three components are calculated as follows:

$$V_{BO,F} = 0.5 f_t A_c, \tag{8}$$

$$V_{PI,F} = 0.918 A_s \sqrt{f_c f_y}, \tag{9}$$

$$V_{FRI} = 0.25 \rho f_y A_c, \tag{10}$$

where f_t is the axial tensile strength of concrete; A_c is the interface area; A_s is the cross-sectional area of the post-installed rebars; f_c is the compressive strength of concrete cubes; f_y is the yield strength of the post-installed rebars; and ρ is the reinforcement ratio of the post-installed rebars.

Considering the influence of vibration disturbance at different curing ages on the shear capacity of the new-to-old concrete interface, a disturbance coefficient K is defined as

$$K = \left(V_{ui}/V_u - 1\right) \times 100\%, \tag{11}$$

where V_{ui} is the average shear capacity of specimens subjected to vibration disturbance, and V_u is the average shear capacity of the reference specimens without vibration.

The calculated disturbance coefficients are listed in Table 6. The variation of the disturbance coefficient with curing age at the onset of vibration is shown in Figure 8. Using the least squares method, the relationship between the disturbance coefficient K and the curing age t can be fitted as

$$K = 1.18t^3 - 13.37t^2 + 35.71t - 1.36. \tag{12}$$

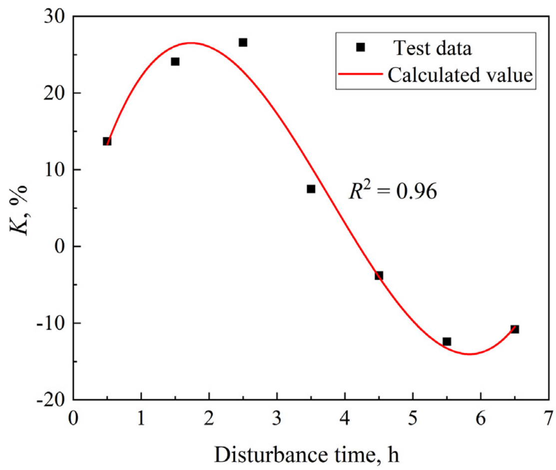

Figure 8. Disturbance coefficient-time curves

Accordingly, the shear capacity of the new-to-old concrete interface considering vibration disturbance can be written as

$$V_u = K\left(0.5 f_t A_c + 0.918 A_s \sqrt{f_c f_y} + 0.25 \rho f_y A_c\right). \tag{13}$$

In this study, the material and geometric parameters are taken as follows: f_t = 2.01 MPa; A_c = 100×100 = 10 000 mm^2; A_s = 2×(3.14×12^2/4) = 226.08 mm^2. Value f_c is taken as the measured compressive strength of concrete cubes listed in Table 3; f_y = 300 MPa, ρ = A_s/A_c×100% = 226.08/10000×100% = 2.26%. The calculated results are summarised in Table 6. The ratio between the experimental shear capacity V_{test}

and the calculated shear capacity V_{calcu} is plotted in Figure 9. The average value of $V_{\text{test}}/V_{\text{calcu}}$ is 0.998, with a maximum value of 1.033, a minimum value of 0.969, and a standard deviation of 0.024, indicating good agreement between the experimental results and the proposed calculation model.

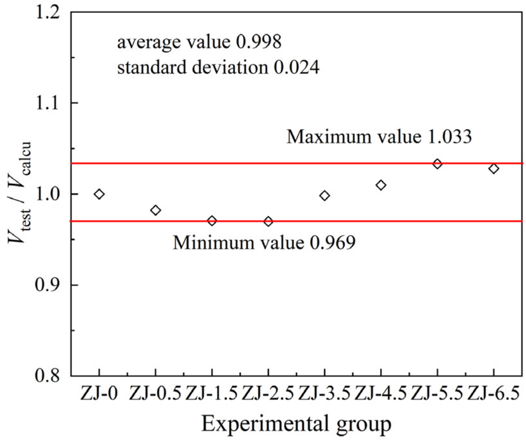

Figure 9. Comparison between the calculation results and the test results

4. Damage stage analysis

4.1. Damage stage analysis based on the energy method

Under external loading, microcracks are generated within the new-to-old concrete specimens. The initiation and propagation of these microcracks release elastic waves, which are captured by the acoustic emission (AE) sensors. By processing the acquired AE signals, waveform data can be obtained, and the area enclosed by the waveform and the coordinate axes represents the AE energy (Tsangouri & Aggelis, 2019). The magnitude of AE energy reflects the amount of released elastic waves and can therefore be used to characterize the cracking and damage evolution of concrete.

The load-time-energy relationships of the specimens in different groups are shown in Figure 10. By comparing the characteristics of the load curves and cumulative AE energy curves, the damage evolution process of the new-to-old concrete specimens can be divided into three distinct stages, namely the elastic stage, the cracked-working stage, and the failure stage, corresponding to stages I, II, and III in Figure 10.

(1) Elastic stage. During this stage, the AE system records only a small amount of energy. The detected AE energy mainly originates from two sources: friction between the specimen and the loading platen, and energy release induced by minor particle dislocation and sliding at the interface. The cumulative AE energy curve exhibits a rapidly increasing trend. At this stage, the shear resistance is primarily provided by the interlocking force and van der Waals force between the new and old concrete. When the applied load approaches the corresponding bearing limit, the interface is about to crack, and the cumulative energy curve shows a sharp increase. For all specimen groups, the cumulative AE energy in this stage is lower than 2000 μs·dB.

(2) Cracked-working stage. Local microcracks initiate at the interface and gradually propagate with increasing load, and the shear resistance is progressively transferred to the post-installed rebars. As the load increases, microcracks propagate in a stable manner without forming through-cracks, and the specimens enter a cracked-working state. During this stage, the cumulative AE energy curve shows a steadily increasing trend. The growth rate of the load with time increases significantly, as indicated by the increased slope of the load curve. With further load increase, partial debonding occurs at the rebar–concrete interface, and cracks within the interface rapidly propagate and coalesce, leading the load curve to reach its peak value. At this moment, due to the instantaneous expansion of a large number of macrocracks, the AE energy release rate increases sharply, and the cumulative energy curve exhibits a steep rise. For all specimen groups, the cumulative AE energy in this stage remains lower than 7110 μs·dB.

(3) Failure stage. In this stage, continuous vertical cracks form along the interface. The load curve drops rapidly; however, owing to the anchoring effect of the post-installed rebars, complete separation between the new and old concrete does not occur. After the interface concrete crushes, frictional sliding between the fractured surfaces still produces a small amount of AE energy, resulting in a slowly increasing cumulative energy curve.

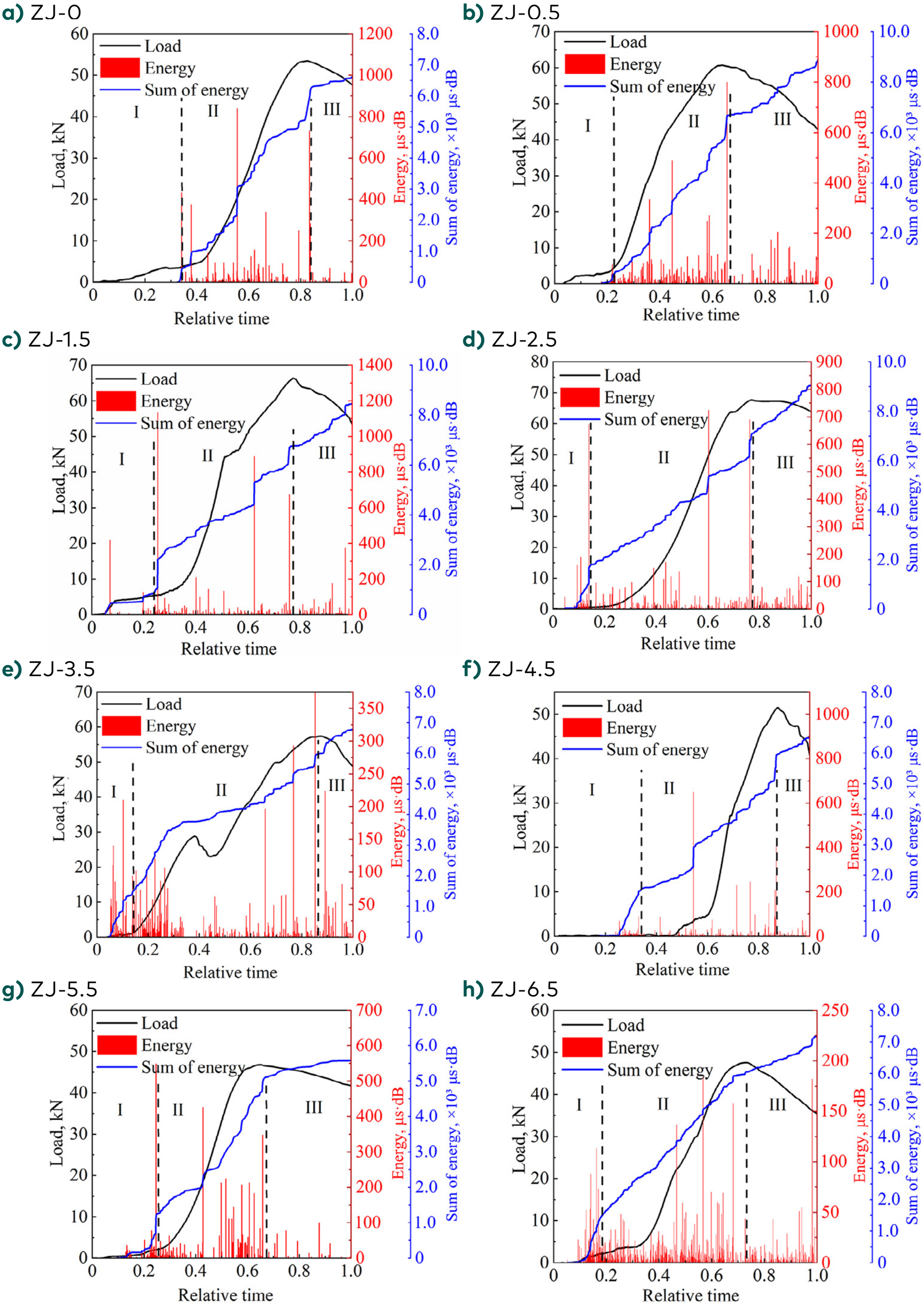

Figure 10. Load- time-energy curves

In addition, Figure 10 shows that the cumulative acoustic emission (AE) energy exhibits pronounced differences among the specimen groups. The cumulative AE energy corresponding to the peak load follows the order: ZJ-2.5 (7110 μs·dB) > ZJ-1.5 (6751 μs·dB) > ZJ-0.5 (6686 μs·dB) > ZJ-3.5 (6363 μs·dB) > ZJ-0 (6155 μs·dB) > ZJ-4.5 (6129 μs·dB) > ZJ-6.5 (5935 μs·dB) > ZJ-5.5 (4686 μs·dB). This trend is consistent with the variation pattern of the shear capacity.

This phenomenon can be explained by the fact that cumulative AE energy essentially reflects the total amount of energy released during the internal damage evolution of the material. Specimens exhibiting higher peak loads (e.g., ZJ-2.5) require greater energy consumption during failure to overcome the bonding strength of the new-to-old concrete interface, resulting in larger cumulative AE energy values. In contrast, specimens subjected to severe initial damage induced by vibration (e.g., ZJ-5.5) experience premature weakening of the interface and the concrete matrix, leading to a significantly reduced total energy release during the failure process.

4.2. Failure mode analysis based on the RA-AF correlation method

The RA-AF correlation method is a classical analytical approach that has been widely applied to fracture mode identification in concrete materials (Bi et al., 2024). In this method, a two-dimensional coordinate system is constructed, in which the ratio of rise time to amplitude, RA (with units of μs/dB), is taken as the horizontal axis, and the ratio of ringing counts to duration, AF (with units of kHz), is taken as the vertical axis. Each coordinate point corresponds to the parameter combination of a single acoustic emission (AE) event.

Elastic waves released during the damage process of concrete materials mainly originate from two mechanisms: (1) crack initiation and propagation, and (2) frictional interaction between crack surfaces. The AE signal characteristics associated with these two mechanisms differ significantly. During crack initiation and propagation, the AE signals exhibit short rise times and are characterized by high AF values and low RA values, commonly referred to as tensile failure. In contrast, during frictional sliding along crack surfaces, the signal duration increases, resulting in low AF values and high RA values, which are commonly referred to as shear failure, as shown in Figure 11.

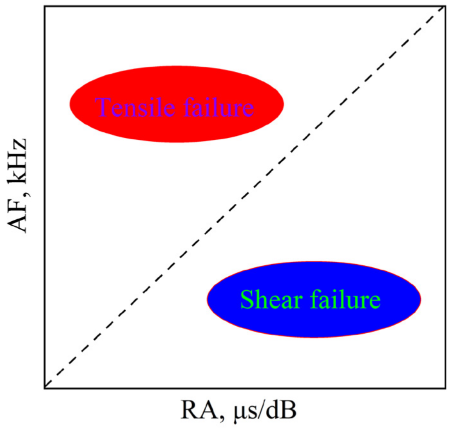

Figure 11. Failure type classification based on RA-AF

Traditional RA-AF correlation analysis has certain limitations, mainly due to the lack of unified standards for coordinate axis scaling, which introduces subjectivity in crack mode classification (Chen et al., 2023). To address this issue, a Gaussian mixture model (GMM) is introduced in this study to cluster the AE data. The probability density function of a single Gaussian model is expressed as

$$N\left(x,\mu,\Sigma_k\right)=\frac{1}{\left(2\pi\right)^{\frac{n}{2}}\cdot\left|\Sigma_k\right|^{\frac{1}{2}}}\exp\left[-\frac{1}{2}\cdot\left(x-\mu\right)^{\tau}\cdot\Sigma_k^{-1}\left(x-\mu\right)\right], \tag{14}$$

where x is an n-dimensional sample vector (column vector); μ is the mean vector, $\sum_k^{-1}$ is the covariance matrix; $\sum_k^{-1}$ denotes the inverse of $\sum_k$; and $(x-\mu)^{\tau}$ represents the transpose of $(x-\mu)$.

By taking a weighted summation of multiple single Gaussian models, a Gaussian mixture model can be obtained, and its probability density function is given by

$$p\left(x_i\right)=\sum_{k=1}^{n}\omega_k p_k\left(x\right)=\sum_{k=1}^{n}\omega_k N\left(x,\mu,\Sigma_k\right), \tag{15}$$

where n is the number of mixture components, and ω_k is the weighting coefficient of the k-th Gaussian component, with the sum of all weights equal to 1.

The model parameters are estimated using the maximum likelihood estimation method, such that the probability density value $J(\theta)$ of the optimal parameter set θ reaches its maximum. The corresponding expressions are

$$\theta=\left[x_i,\mu_i,\Sigma_i\right], i=1,2,3,\ldots,n. \tag{16}$$

$$\ln J(\theta)=\ln\left[\prod_{i=1}^{n}p(x_i)\right]=\sum_{i=1}^{n}\ln p(x_i)=\sum_{k=1}^{n}\ln\left[\omega_k N\left(x;\mu;\sigma_k^2\right)\right]. \tag{17}$$

In this study, AE parameters recorded prior to specimen failure are analysed. The clustering results obtained using the Gaussian mixture model are shown in Figure 12. In the figure, red event points represent tensile failure modes, with classification boundaries of RA values ranging from 0 to 3 μs/dB and AF values ranging from 0 to 200 kHz. Blue event points represent shear failure modes, with classification boundaries of RA values ranging from 3 to 80 μs/dB and AF values ranging from 0 to 125 kHz.

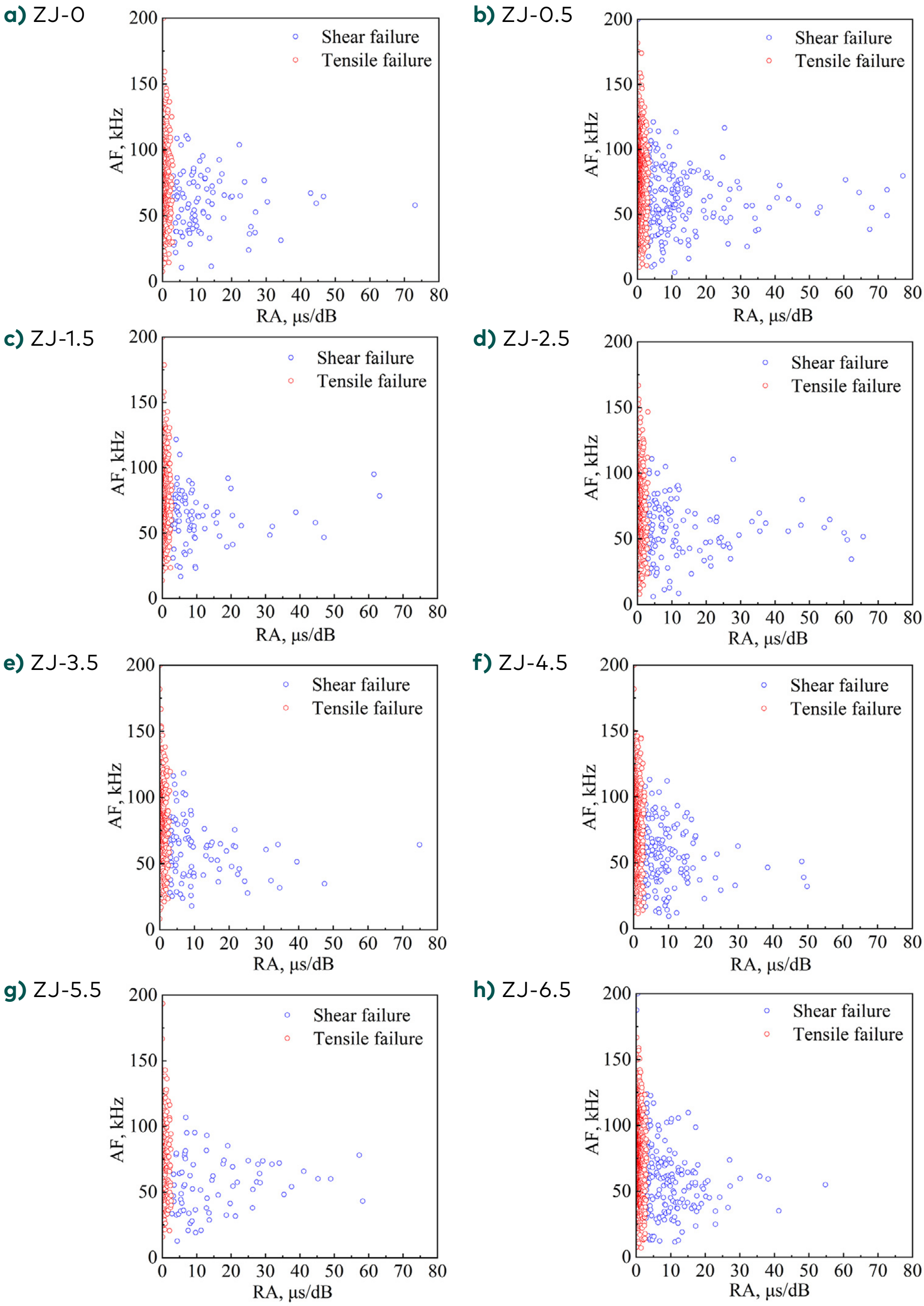

Figure 12. Failure mode

The relationships between the occurrence rates of tensile and shear failure events and the stress level for different specimen groups are illustrated in Figure 13. As shown in the figure, the occurrence rates of both failure modes increase with increasing stress level. The occurrence rate of tensile failure events exhibits a rapid growth trend as the stress level increases and remains dominant throughout the entire loading process. In contrast, the increase in shear failure events is relatively gradual.

The occurrence rate of shear failure events remains consistently below 25%, indicating that the damage evolution of the new-to-old concrete specimens is characterized by a pronounced tensile-dominated failure mechanism. This behaviour can be attributed to the fact that, under shear loading, tensile-type microcracks preferentially initiate at the new-to-old concrete interface. Shear failure is activated only after these cracks propagate and coalesce, allowing frictional sliding to occur along the crack surfaces.

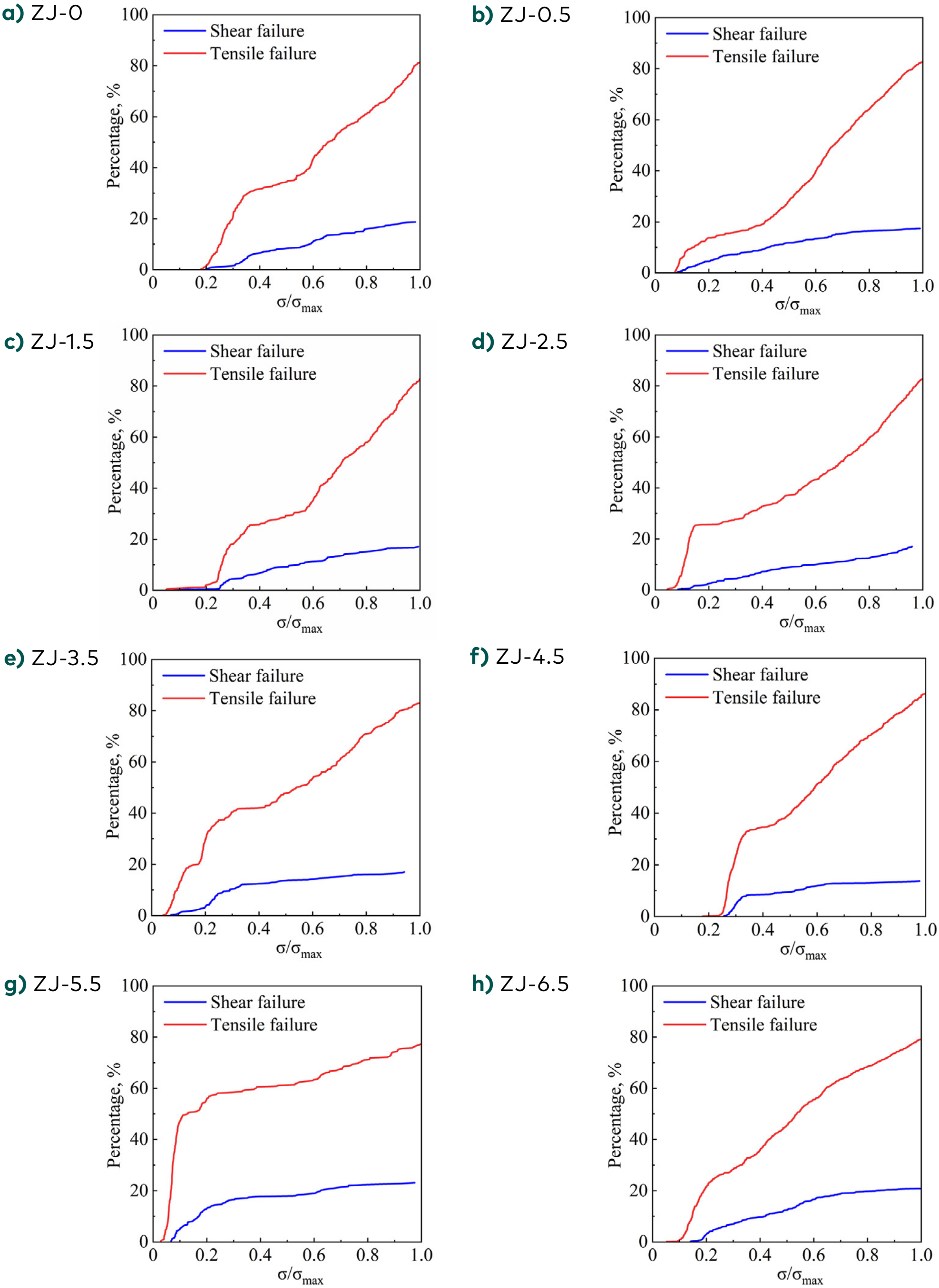

Figure 13. Event rates – stress levels curves

The variations in the rise time of acoustic emission (AE) signals corresponding to the two failure modes under different stress levels for each specimen group are shown in Figure 14. As indicated in the figure, the AE signal rise times associated with tensile and shear failure modes exhibit pronounced differences.

The rise times of tensile failure signals are mainly distributed within the range of 0–200 μs, whereas the rise times of shear failure signals span a much wider range, reaching up to one order of magnitude greater than those of tensile failure signals. This distinction arises from the fundamentally different energy release and wave propagation mechanisms associated with the two failure modes. Tensile failure induces microcrack initiation accompanied by transient volumetric deformation in the concrete, and the released energy propagates rapidly in the form of longitudinal waves along the direction of particle vibration. In contrast, shear failure releases energy through sliding and friction along crack surfaces, with energy propagation dominated by transverse waves traveling in directions perpendicular to particle motion.

Since the propagation velocity of longitudinal waves is significantly higher than that of transverse waves, and the frictional effects involved in shear failure prolong the energy release process, AE signals associated with shear failure exhibit longer rise time characteristics.

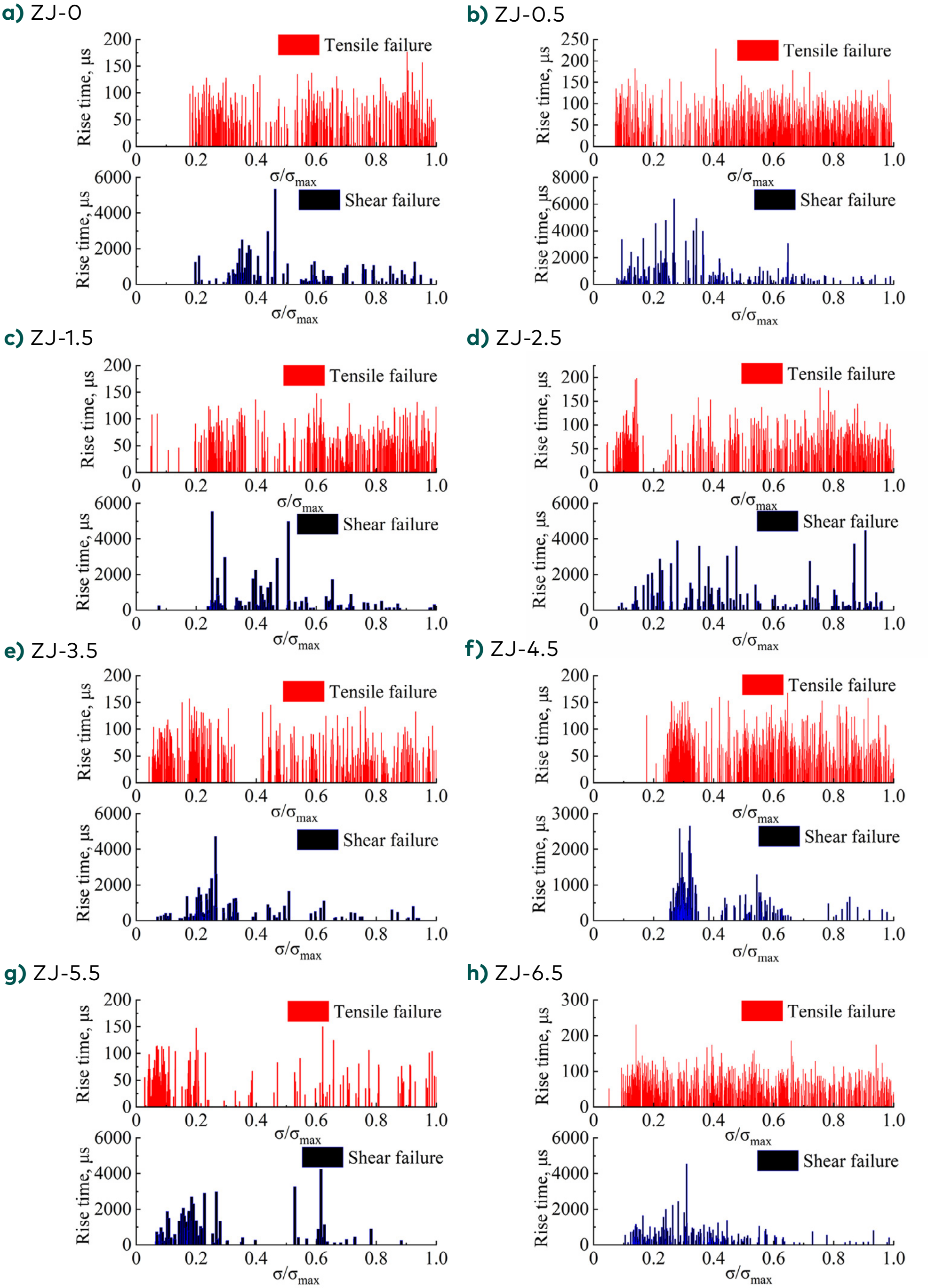

Figure 14. Rise time – stress levels curves

4.3. Damage type analysis based on the fuzzy C-means method

The fuzzy *C*-means (FCM) algorithm is a classical soft clustering method, whose core concept is to determine the optimal cluster centers C_i through an iterative optimization process by minimizing the weighted sum of squared distances between samples and the cluster centers (Li & Wang, 2023). Using this method, damage type analysis of acoustic emission (AE) signals from new-to-old concrete specimens can be effectively performed. The objective function $J(U,V)$, which represents the weighted sum of squared distances to the cluster centers C_i, is expressed as

$$J(U,V)=\sum_{j=1}^{n}\sum_{i=1}^{m}\left[u_i\left(x_j\right)\right]^f d^2\left(x_j,C_i\right). \tag{18}$$

The membership matrix U and the cluster centre matrix V are defined as

$$U=\begin{pmatrix} u_1\left(x_1\right) & \dots & u_1\left(x_n\right) \\ \vdots & \ddots & \vdots \\ u_m\left(x_1\right) & \cdots & u_m\left(x_n\right) \end{pmatrix}, \tag{19}$$

$$V=\left[C_1 \;\; C_2 \;\; \cdots \;\; C_m\right], \tag{20}$$

where $u_i(x_j)$ denotes the membership degree of the j-th data point belonging to the i-th cluster.

The membership degrees satisfy the constraint

$$\sum_{i=1}^{m}u_i\left(x_j\right)=1 \qquad \forall j. \tag{21}$$

In this study, the FCM algorithm is applied to cluster the AE amplitude and peak frequency of the new-to-old concrete specimens. The clustering results are shown in Figure 15. Three distinct damage types are identified, namely Type I, Type II, and Type III. The damage mechanisms of the new-to-old concrete specimens mainly include crack initiation and propagation at the interface, crack initiation and propagation within the concrete matrix of the new and old concrete, and tensile yielding of the embedded steel rebars.

Taking specimen ZJ-0 as an example, the correspondence between the clustered damage types and the actual damage mechanisms of the specimen is further illustrated in the following analysis.

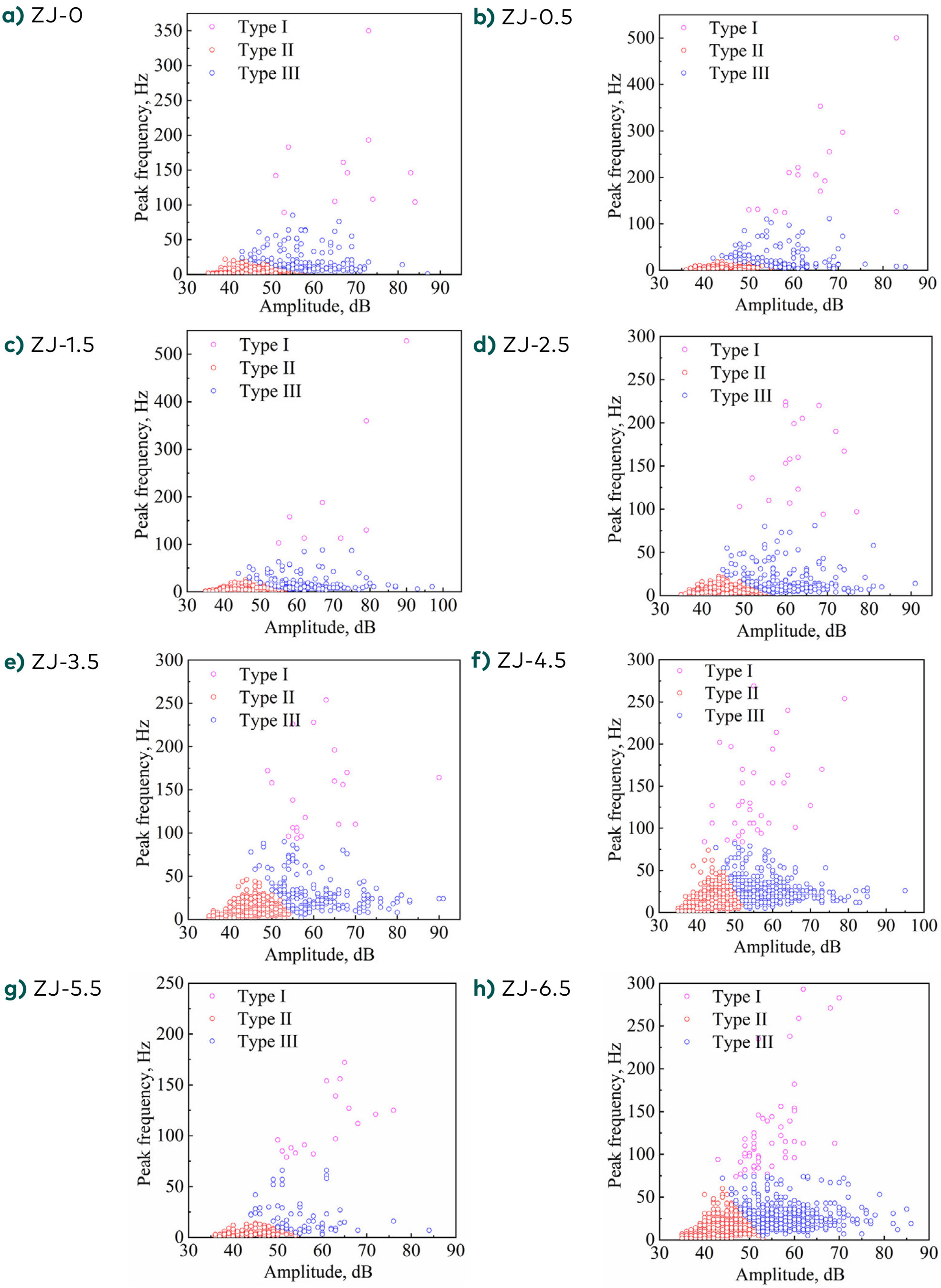

Figure 15. Damage type

Table 7. Average value of AE parameters

Type	Rise time, μs	Ring count	Amplitude, dB	Peak frequency, kHz
I	3119.89	393.68	65.21	206.11
II	62.31	19.19	44.13	5.56
III	238.92	74.62	59.57	19.32

The average values of the AE signal characteristic parameters corresponding to Type I, Type II, and Type III damage for specimen ZJ-0 are summarised in Table 7. In terms of the magnitudes of these parameters, an overall relationship of Type I > Type III > Type II is observed. AE signals generated by damage to steel reinforcement typically exhibit frequency components in the range of 100–300 kHz, which is consistent with the frequency characteristics of Type I signals. This indicates that Type I damage corresponds to damage of the embedded steel rebars.

For Type II and Type III signals, which exhibit similar frequency characteristics below 20 kHz, further discrimination of damage types requires consideration of the material characteristics of concrete. The interfacial transition zone between new and old concrete is relatively weak, which constrains energy release during cracking and results in low-frequency AE signals, corresponding to Type II damage. In contrast, the concrete matrix generally exhibits better material integrity than the interface. During crack propagation within the matrix, the damage evolution occurs in a more homogeneous medium. Although the frequency range is similar, the damage mechanism differs, corresponding to the AE characteristics of Type III.

In addition, Figure 15 shows that, in terms of the number of AE events, the occurrence follows the order Type II > Type III > Type I. This indicates that damage in the new-to-old concrete specimens predominantly occurs at the interface, while damage-related AE signals associated with the steel rebars are mainly generated at the final loading stage when yielding of the rebars takes place.

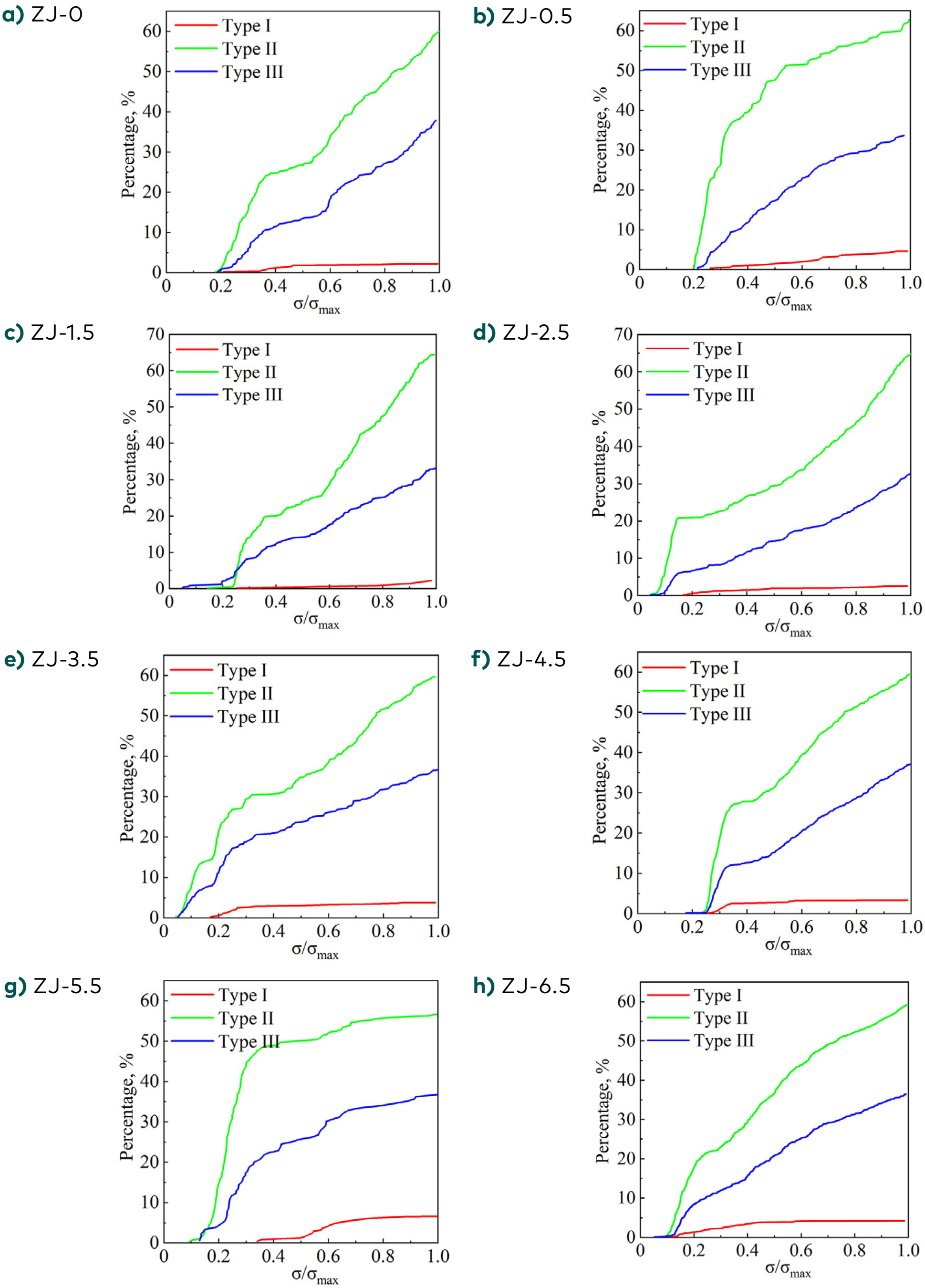

Figure 16. Damage proportion – stress levels curves

Table 8. Damage proportion

Number	Type I, %	Type II, %	Type III, %
ZJ-0	2.2	60.0	37.8
ZJ-0.5	3.5	62.8	33.7
ZJ-1.5	2.2	64.4	33.4
ZJ-2.5	2.5	64.8	32.7
ZJ-3.5	3.8	59.7	36.5
ZJ-4.5	3.3	59.2	37.5
ZJ-5.5	6.5	56.7	36.8
ZJ-6.5	4.2	59.6	36.2

Figure 16 illustrates the variation in the proportions of different damage types with increasing loading stress level, and the damage proportion data at specimen failure are summarized in Table 8. The results indicate that damage evolution during the loading process is mainly governed by two modes: crack initiation and propagation at the interface (Type II) and crack initiation and propagation within the concrete matrix (Type III). The combined proportion of these two damage types exceeds 90% of the total damage, whereas steel reinforcement damage (Type I) contributes less than 10% of the total AE events.

Vibration disturbance applied at different curing ages significantly alters the damage characteristics of the specimens. During the early setting stage (ZJ-0 to ZJ-4.5), the proportion of Type II damage first increases and then decreases with increasing curing age. During the transition stage from initial setting to final setting (ZJ-5.5 to ZJ-6.5), although the proportion of interfacial damage increases, its peak value remains lower than that of the reference specimen.

This behaviour can be attributed to the differentiated effects of vibration disturbance at different curing ages on the initial defects at the new-to-old concrete interface. For specimen ZJ-2.5, a relatively low density of initial microcracks and a dense concrete matrix structure lead to the generation of a higher proportion of Type II damage events at the interface. In contrast, specimen ZJ-5.5 experiences a higher density of initial microcracks in the concrete matrix due to vibration disturbance. Under external loading, matrix crack propagation is more readily activated, which reduces the proportion of Type II damage events.

Conclusions

Based on the experimental investigation and acoustic emission analysis of new-to-old concrete specimens subjected to vibration disturbance, the following conclusions can be drawn:

(1) Vibration disturbance has a significant influence on the compressive strength of concrete cubes at different curing ages. Vibration applied within the first 2.5 h during the early setting stage enhances compressive strength, while vibration applied in the middle and later periods of the transition stage from initial setting to final setting leads to a slight increase. In contrast, vibration applied at other curing ages results in a reduction in compressive strength. The variation trend of the interfacial shear capacity is generally consistent with that of the compressive strength of concrete cubes. A modified shear capacity model incorporating a vibration disturbance coefficient is proposed, and the calculated results show good agreement with the experimental data. These findings indicate that allowing traffic during the early setting stage is beneficial for improving the shear capacity of the interface between new and old bridge structures.

(2) Based on the characteristics of cumulative acoustic emission energy and load variation, the damage evolution process of new-to-old concrete specimens can be divided into three stages: the elastic stage, the cracked-working stage, and the failure stage. The cumulative AE energy corresponding to the peak load exhibits the same variation trend as the interfacial shear capacity for all specimen groups.

(3) According to the RA-AF correlation analysis, the failure mode of new-to-old concrete specimens is predominantly tensile in nature. The occurrence rate of tensile failure events exceeds 75% and increases rapidly with increasing loading stress. The rise time of tensile failure signals is mainly distributed within the range of 0–200 μs.

(4) Based on the fuzzy C-means clustering analysis, damage evolution of new-to-old concrete specimens is mainly characterised by crack initiation and propagation at the interface and within the concrete matrix, with their combined proportion exceeding 90% of the total damage. For all specimen groups, the proportion of interfacial damage initially increases and then decreases during the early setting stage, while a slight increase is observed during the transition stage from initial setting to final setting; however, the overall proportion remains lower than that of the reference specimens.

Funding

This research was funded by Sichuan Science and Technology Program (grant No. 2024YFTX0037).

Disclosure Statement

We declare that have no known competing financial interests or personal relationships that could have appeared to influence the work reported in this paper.

Statement of the use of generative AI and AI-assisted technologies in the writing process

In the preparation of this manuscript, no AI technologies were used for text generation, data interpretation, figure creation, reference recommendation, or any other aspect of the research or writing process. All scientific content, data analysis, and conclusions are entirely the original work of the authors.

REFERENCES

Bai, M., Ding, T., Zhao, Y., & Zhao, Y. (2024). Shear performance of new-to-old concrete interface based on various surface preparation techniques and roughness. *Case Studies in Construction Materials*, *21*, Article e03549. https://doi.org/10.1016/j.cscm.2024.e03549

Bi, J., Zhao, Y., Wu, Z., Li, J., & Wang, C. (2024). Research on crack classification method and failure precursor index based on RA-AF value of brittle rock. *Theoretical and Applied Fracture Mechanics*, *129*, Article 104179. https://doi.org/10.1016/j.tafmec.2023.104179

Cattaneo, S., Zorzato, G., & Bonati, A. (2021). Assessing method of shear strength between old to new concrete interface under cycling loading. *Construction and Building Materials*, *309*, Article 125160. https://doi.org/10.1016/j.conbuildmat.2021.125160

Chen, Z., Zhang, G., He, R., Tian, Z., Fu, C., & Jin, X. (2023). Acoustic emission analysis of crack type identification of corroded concrete columns under eccentric loading: A comparative analysis of RA-AF method and Gaussian mixture model. *Case Studies in Construction Materials*, *18*, Article e02021. https://doi.org/10.1016/j.cscm.2023.e02021

Daneshvar, D., Behnood, A., & Robisson, A. (2022). Interfacial bond in concrete-to-concrete composites: A review. *Construction and Building Materials*, *359*, Article 129195. https://doi.org/10.1016/j.conbuildmat.2022.129195

Editorial Department of China Journal of Highway and Transport. (2024). Review on China's bridge engineering research: 2024. *China Journal of Highway and Transport*, *37*(12), 1–160. https://doi.org/10.19721/j.cnki.1001-7372.2024.12.001

Feng, S., Xiao, H., & Geng, J. (2020). Bond strength between concrete substrate and repair mortar: Effect of fibre stiffness and substrate surface roughness. *Cement and Concrete Composites*, *114*, Article 103746. https://doi.org/10.1016/j.cemconcomp.2020.103746

Gu, P., Wu, H., Li, L., Li, Z., Hong, J., & Zhuang, M.-L. (2024). Effect of traffic vibration on compressive strength of high-strength concrete and tensile strength of new-to-old concrete interfaces. *Buildings*, *14*(12), Article 3765. https://doi.org/10.3390/buildings14123765

Huang, H., Jiang, B., Guo, T., Fang, M., Wang, T., Tu, Y., Ji, Y., Wang, C., & Sas, G. (2025). New insights into the interfacial shear behavior of new-to-old concrete: A molecular dynamics simulation study. *Construction and Building Materials*, *471*, Article 140691. https://doi.org/10.1016/j.conbuildmat.2025.140691

Ibrahim, A., Abdelkhalek, S., Zayed, T., Qureshi, A. H., & Mohammed Abdelkader, E. (2024). A comprehensive review of the key deterioration factors of concrete bridge decks. *Buildings*, *14*(11), Article 3425. https://doi.org/10.3390/buildings14113425

Jang, H.-O., Lee, H.-S., Cho, K., & Kim, J. (2017). Experimental study on shear performance of plain construction joints integrated with ultra-high performance concrete (UHPC). *Construction and Building Materials*, *152*, 16–23. https://doi.org/10.1016/j.conbuildmat.2017.06.156

Júlio, E., Dias-da-Costa, D., Branco, F. A. B., & Alfaiate, J. M. V. (2010). Accuracy of design code expressions for estimating longitudinal shear strength of strengthening concrete overlays. *Engineering Structures*, *32*(8), 2387–2393. https://doi.org/10.1016/j.engstruct.2010.04.013

Kocáb, D., Topolář, L., Kucharczyková, B., & Halamová, R. (2019). The analysis of acoustic emission signals detected during the loading of cement-based materials. *Engineering Failure Analysis*, *99*, 18–25. https://doi.org/10.1016/j.engfailanal.2019.01.002

Li, H., & Wang, J. (2023). From soft clustering to hard clustering: A collaborative annealing fuzzy *c*-means algorithm. *IEEE Transactions on Fuzzy Systems*, *32*(3), 1181–1194. https://doi.org/10.1109/TFUZZ.2023.3319663

Li, S., Lv, H., Huang, T., Zhang, Z., Yao, J., & Ni, X. (2022). Degradation of reinforced concrete beams subjected to sustained loading and multi-environmental factors. *Buildings*, *12*(9), Article 1382. https://doi.org/10.3390/buildings12091382

Li, X., Miao, T., Liu, T., Chen, R., & Yu, A. (2025). Acoustic emission evaluation and localization correction of concrete damage considering stress levels. *Case Studies in Construction Materials*, *22*, Article e04281. https://doi.org/10.1016/j.cscm.2025.e04281

Lin, Y., Xu, W., Zhang, X., & Liu, K. (2021). Shear mechanism and bond strength calculation of new-to-old concrete interface with anchor bars. *Industrial Construction*, *51*(6), 72–83.

Liu, Q., Ma, J., Qiao, P., Wu, E., & Zhou, G. (2024). Mesoscale modeling of new-to-old concrete interface under combined shear and compressive loads. *Engineering Fracture Mechanics*, *307*, Article 110331. https://doi.org/10.1016/j.engfracmech.2024.110331

Maili, C., & Jing, M. (2018). Experimental study on shear behavior of the interface between new and old concrete with reinforced. *KSCE Journal of Civil Engineering*, *22*(5), 1882–1888. https://doi.org/10.1007/s12205-017-2007-6

Ministry of Transport of the People's Republic of China. (2015). General Specifications for Design of Highway Bridges and Culverts (JTG D60-2015). Beijing, China.

Ministry of Transport of the People's Republic of China. (2018). Specifications for Design of Highway Reinforced Concrete and Prestressed Concrete Bridges and Culverts (JTG 3362-2018). Beijing, China.

Momayez, A., Ehsani, M. R., Ramezanianpour, A. A., & Rajaie, H. (2005). Comparison of methods for evaluating bond strength between concrete substrate and repair materials. *Cement and Concrete Research*, *35*(4), 748–757. https://doi.org/10.1016/j.cemconres.2004.05.027

Qiao, Y., Zhang, W., Cheng, J., Tong, L., Sun, C., Deng, J., & Ge, F. (2025). Experimental and theoretical investigations on the bond–slip behavior of newly poured concrete and reinforcement bars under traffic-induced vibrations in bridge widening. *International Journal of Concrete Structures and Materials*, *19*, 84. https://doi.org/10.1186/s40069-025-00820-1

Santos, D. S., Santos, P. M., & Dias-da-Costa, D. (2012). Effect of surface preparation and bonding agent on the concrete-to-concrete interface strength. *Construction and Building Materials*, *37*, 102–110. https://doi.org/10.1016/j.conbuildmat.2012.07.028

Shao, C., Yan, H., Chen, L., Xu, Y., & Cao, S. (2019). Widening and strengthening of the Songpu bridge. *Structural Engineering International*, *29*(3), 354–361. https://doi.org/10.1080/10168664.2019.1601052

Tsangouri, E., & Aggelis, D. G. (2019). A review of acoustic emission as indicator of reinforcement effectiveness in concrete and cementitious composites. *Construction and Building Materials*, *224*, 198–205. https://doi.org/10.1016/j.conbuildmat.2019.07.042

Wei, J., Fu, Z., & Zhang, J. (2016). Effect of traffic load induced bridge vibration on adherence of new and old concrete. *Journal of Highway and Transportation Research and Development*, *33*(05), 61–65.

Xu, Y., Zeng, Z., Wang, Z., & Yan, H. (2021). Seismic study of a widened and reconstructed long-span continuous steel truss bridge. *Structure and Infrastructure Engineering*, *17*(2), 191–201. https://doi.org/10.1080/15732479.2020.1733621

Yan, B., Zhang, W., Ye, Y., & Yi, W. (2025). Study on the prediction of shear capacity of new and old concrete interfaces based on explainable machine learning algorithms. *Structures*, *71*, Article 108065. https://doi.org/10.1016/j.istruc.2024.108065

Zanotti, C., & Randl, N. (2019). Are concrete-concrete bond tests comparable? *Cement and Concrete Composites*, *99*, 80–88. https://doi.org/10.1016/j.cemconcomp.2019.02.012

Zhou, J., Zhou, Z., Zhang, L., Zhang, J., & Shi, X. (2023). Traffic-induced vibrations at the wet joint during the widening of concrete bridges and non-interruption traffic control strategies. *Computers and Concrete*, *32*(4), Article 411.